Review of Scientific Instruments

RESEARCH ARTICLE | NOVEMBER 11 2024

Frequency-domain instrument with custom ASIC for dual-slope near-infrared spectroscopy

Alper Kılıç ; Giles Blaney ; Fatemeh Tavakoli ; Jodee Frias ; Angelo Sassaroli ; Sergio Fantini ; Valencia Koomson

Check for updates

Rev. Sci. Instrum. 95, 114706 (2024)
https://doi.org/10.1063/5.0227363

View Online
Export Citation

Articles You May Be Interested In

An Analog Low-Power Frequency Readout ASIC for a SAW Array

AIP Conference Proceedings (November 2011)

Development of a low-energy charged particle detector with on-anode ASIC for in-situ plasma measurement in the Earth's magnetosphere

AIP Conference Proceedings (June 2009)

EB60: An advanced direct wafer exposure electron-beam lithography system for high-throughput, high-precision, submicron pattern writing

J. Vac. Sci. Technol. B (January 1987)

20 March 2025 18:15:16

Nanotechnology & Materials Science
Optics & Photonics
Impedance Analysis
Scanning Probe Microscopy
Sensors
Failure Analysis & Semiconductors

Unlock the Full Spectrum.
From DC to 8.5 GHz.
Your Application. Measured.

Find out more

Zurich Instruments

AIP Publishing

Review of Scientific Instruments ARTICLE pubs.aip.org/aip/rsi

Frequency-domain instrument with custom ASIC for dual-slope near-infrared spectroscopy

Cite as: Rev. Sci. Instrum. 95, 114706 (2024); doi: 10.1063/5.0227363
Submitted: 8 July 2024 • Accepted: 14 October 2024 •
Published Online: 11 November 2024

View Online Export Citation CrossMark

Alper Kılıç,[1,a] Giles Blaney,[2] Fatemeh Tavakoli,[2] Jodee Frias,[2] Angelo Sassaroli,[2] Sergio Fantini,[2] and Valencia Koomson[1]

AFFILIATIONS

[1] Department of Electrical and Computer Engineering, Tufts University, 161 College Avenue, Medford, Massachusetts 02155, USA
[2] Department of Biomedical Engineering, Tufts University, 4 Colby Street, Medford, Massachusetts 02155, USA

[a] Author to whom correspondence should be addressed: alper.kilic@tufts.edu

ABSTRACT

Real-time and non-invasive measurements of tissue concentrations of oxyhemoglobin (HbO_2) and deoxyhemoglobin (HbR) are invaluable for research and clinical use. Frequency-domain near-infrared spectroscopy (FD-NIRS) enables non-invasive measurement of these chromophore concentrations in human tissue. We present a small form factor, dual-wavelength, miniaturized FD-NIRS instrument for absolute optical measurements, built around a custom application-specific integrated circuit and a dual-slope/self-calibrating (DS/SC) probe. The modulation frequency is 55 MHz, and the heterodyning technique was used for intensity and phase readout, with an acquisition rate of 0.7 Hz. The instrument consists of a 14 × 17 cm^2 printed circuit board (PCB), a Raspberry Pi 4, an STM32G491 microcontroller, and the DS/SC probe. The DS/SC approach enables this instrument to be selective to deeper tissue and conduct absolute measurements without calibration. The instrument was initially validated using a tissue-mimicking solid phantom, and upon confirming its suitability for *in vivo*, a vascular occlusion experiment on a human subject was conducted. For the phantom experiments, an average of 0.08° phase noise and 0.10% standard deviation over the mean for the intensities was measured at a source–detector distance of 35 mm. The absorption and reduced scattering coefficients had average precisions (variation of measurement over time) of 0.5% and 0.9%, respectively, on a window of ten frames. Results from the *in vivo* experiment yielded the expected increase in HbO_2 and HbR concentration for all measurement types tested, namely SC, DS intensity, and DS phase.

Published under an exclusive license by AIP Publishing. https://doi.org/10.1063/5.0227363

20 March 2025 18:15:16

I. INTRODUCTION

Near-infrared spectroscopy (NIRS) is an optical non-invasive method for measuring the optical properties of turbid media by illuminating the medium with a light source at one location and then collecting the diffused light at some distance, usually a few centimeters away from the illumination point.[1] For traditional single-distance (SD) reflectance NIRS, the measurement is representative of a banana-shaped region of sensitivity to absorption change beneath the SD set.[2,3] The further the source and detector are spaced, the deeper the light permeates. For a source–detector separation of 30 mm in a medium with $\mu_a \sim 0.01\ mm^{-1}$ and $\mu_s' \sim 1.0\ mm^{-1}$, the mean penetration depth is on the order of 5–10 mm depending on the instrument and the medium.[4] Frequency-domain near-infrared spectroscopy (FD-NIRS) measures the intensity (I) and phase (ϕ) of detected photon density waves.[5] Changes in either just I or ϕ may be converted to changes in the absorption coefficient ($\Delta\mu_a$) and then changes in the concentrations of hemoglobin.[6] Alternatively, the spatial dependence of both I and ϕ may be converted into absolute optical properties, the absorption coefficient, and the reduced scattering coefficient (μ_a and μ_s', respectively).[7]

In biomedical applications, the wavelength of the light source is usually between 650 and 900 nm since this is an optical window associated with low water absorption in biological tissue.[4] In this wavelength range, many chromophores such as water, lipid, melanin,[8] and bilirubin interact with the light, but oxyhemoglobin (HbO_2) and deoxyhemoglobin (HbR) dominate μ_a, allowing recovery of their concentrations from optical measurements of μ_a.[9] The measurements we made on human subjects were focused on finding changes in concentrations of dynamically changing chromophores. The only chromophores that we are sensitive to in this wavelength range that change dynamically are HbO and HbR during a venous

Published under an exclusive license by AIP Publishing

occlusion. The non-invasive nature of NIRS, coupled with the existence of this optical window, makes NIRS a very attractive technique for biomedical researchers. As a result, NIRS has been used in many clinical studies focused on pediatrics,[10] breast cancer,[11] functional brain imaging,[1,5] neonatal care,[12] ischemia,[13] ulcers,[14] and peripheral artery disease,[15] to name a few.

There are three main NIRS methods, namely continuous-wave (CW-NIRS),[16] time-domain (TD-NIRS),[17] and frequency-domain (FD-NIRS).[5] The distinguishing feature of these methods is whether/how the light source is modulated. The simplest implementation is CW-NIRS, where the light source is not modulated. In CW-NIRS, the medium is illuminated by a light source with constant intensity, and temporal changes in the detected intensity are recorded. From these changes, one may recover absorption changes due to tissue hemodynamics or other physiological processes ($\Delta\mu_a$), but absolute values for μ_a and μ_s' must be assumed. Contrary to CW-NIRS, the intensity of the light source is modulated in the two other methods. For TD-NIRS, this modulation results in a very short pulse (on the order of a pico-second), whereas for FD-NIRS the light source is modulated as a sine wave in the radio frequencies (50–1000 MHz). This modulation makes the light intensity a function of time; therefore, it becomes possible to compute the average time it takes for the photons to travel through the media. These additional degrees of freedom make it possible to recover absolute values of μ_a and μ_s', given that the system is properly calibrated. As a result, TD-NIRS and FD-NIRS methods can recover the absolute concentrations of HbO_2 ($[HbO_2]$) and HbR ([HbR]), whereas CW-NIRS methods can only recover the change of these chromophores' concentrations over time (given assumed values of μ_a and μ_s'). This added capability of TD-NIRS or FD-NIRS comes with extra hardware and data analysis complexity. For TD-NIRS, commercially available pico-second laser sources are generally quite expensive and bulky. In addition, to resolve the recovered light, photodetectors also need to be high-speed. Hardware complexity for FD-NIRS, however, is relatively relaxed. One can use off-the-shelf laser diodes and photodetectors to build an FD-NIRS instrument.

Even though there are many CW-NIRS solutions available on the market, such as the ones integrated into smartwatches, currently ISS (Urbana-Champaign, USA) offers the only commercially available frequency domain instruments.[18,19] However, many academic research groups have designed frequency domain devices. Some of these designs leverage commercial vector network analyzers (VNAs) in order to extract the intensity and phase information,[20–23] whereas some other designs use the direct sampling approach, where analog-to-digital converters (ADCs) with high sampling rates interface with the high frequency signals directly.[24–27] Direct sampling is not the only solution that has been investigated. Instead of handling the high frequency signals directly, some other groups have utilized the homodyne approach, where the recovered high frequency signals are mixed with a local oscillator (LO) of the same frequency and an I–Q demodulation scheme is used to extract the phase and intensity information.[28–32] Another solution a few groups have chosen is the heterodyne approach,[23,33–40] where the recovered signals are mixed with an LO signal that is at a slightly different frequency. Heterodyne mixing preserves the intensity and phase shift information while translating this information to a much lower carrier frequency, where sampling is easier.

Although all of these approaches have proven to be successful, not all of them are conducive to portable and cost-effective instruments. For instance, VNAs are rather expensive and bulky benchtop equipment, and the high sampling rate ADCs that are required for the direct sampling approach consume a lot of power by themselves. They also usually require a Field Programmable Gate Array (FPGA) to drive them, which makes this approach even more power-hungry. On the other hand, there are also integrated attempts that show more promise toward wearability and portability.[41–43] Therefore, in our efforts, we chose the heterodyne approach in an integrated platform. In the past, we had presented a few different iterations of our efforts, improving integration with each iteration.[44–50] Recently, we had designed and demonstrated a dual-wavelength, heterodyne FD-NIRS instrument.[51] The instrument consisted of a three stack printed circuit board (PCB) (12 ×11.5× 5 cm^3) and featured a custom-designed application specific integrated circuit (ASIC) in a 130 nm IBM process[52] along with a multi-distance probe. The heterodyne output signals were sampled via a data acquisition system (DAQ, National Instruments Corp., Austin, TX, USA). In this work, we combine heterodyne FD-NIRS (performed by the ASIC[52]) with the dual-slope approach, which is a specialized multi-distance method. Furthermore, we improve our previous work by reducing the size to only a single PCB of 14 × 17 cm^2, leaving only the readout and analysis blocks off-board for which we use compact commercial solutions instead of a full sized DAQ. The resulting instrument is compact and portable due to its high level of integration compared to most of the reported works, where the solutions include either large discrete RF components,[28,31,32,35,39] instrument mounted on racks,[29,34,36–38,40] or VNA based instruments.[20–23] Additionally, we remove the need for calibration by employing the self-calibrating[53]/dual-slope[6,54] (SC/DS) geometry. The SC/DS configuration removes the need for phantom calibration, which is performed regularly and is necessary for typical FD-NIRS systems intending to measure absolute μ_a and μ_s'. The particulars of SC, DS, and FD-NIRS theory will be discussed in Sec. II. In Sec. III, we describe the hardware development, block by block. In Sec. IV, we present our results with phantoms and *in vivo* human measurements during vascular occlusion.

II. FREQUENCY-DOMAIN NEAR-INFRARED SPECTROSCOPY THEORY

A. Measurements of absolute absorption and reduced scattering coefficients: The self-calibrating (SC) method

In FD-NIRS, the estimation of the absolute optical properties, namely μ_a and μ_s', can be obtained by multi-distance,[55] multi-frequency measurements,[23] or even single-distance and single-frequency measurements,[56] after proper calibration. Typically, these strategies require previous calibration on a phantom with known optical properties. At least two shortcomings of this phantom calibration approach can be mentioned,

- one must assume that the coupling between each optode and the medium remains unchanged between calibration and measurement on an unknown medium and,
- one must also assume that the laser's output power and/or the detector's gain do not change between calibration and measurement.

20 March 2025 18:15:16

Published under an exclusive license by AIP Publishing

These prerequisites are difficult to satisfy, especially during *in vivo* measurements. A more robust approach adopted in this work is the SC method.[53] This method uses a probe with two sources (S_1 and S_2) and two detectors (D_1 and D_2) (see Fig. 1). Several configurations of the optodes are possible,[57] but all of them must satisfy one fundamental property: that the closest detector to S_1 (i.e., D_1) is also the farthest detector from S_2, and vice versa: the farthest detector from S_1 (i.e., D_2) is the closest detector to S_2.[57] In addition, it must be verified that

$$\overline{S_1D_2} - \overline{S_1D_1} = \overline{S_2D_1} - \overline{S_2D_2} = \Delta r, \tag{1}$$

where Δr is the difference between long and short distances. The method relies on both measurements of ϕ (phase) and I (intensity) data types for all the possible combinations of source–detector pairs [i.e., four single-distance (SD) measurements per each data type]. A single-slope (SS) measurement is identified by one source and two detectors (e.g., $S_1D_1D_2$), and it is defined by

$$SS = \frac{\Delta Y}{\Delta r} = \frac{Y(r_2) - Y(r_1)}{\Delta r}, \tag{2}$$

where Y is either ϕ or the logarithmic intensity $\ln[r^2 I]$ (where r is source detector distance), and source–detector distances r_1 and r_2 are defined as

$$r_1 = \overline{S_1D_1}, \tag{3}$$

$$r_2 = \overline{S_1D_2}. \tag{4}$$

In other words, one SS measurement is defined by using two SD measurements relative to the same source. If I and ϕ data were calibrated, one SS measurement of both data types would be enough to measure the optical properties.[7,55,58] This is impossible without calibration because the optodes coupling to the medium and the gains of the detectors are unknown. However, when both SS measurements are averaged $[(SS_1 + SS_2)/2]$, all the unknowns related to source emission, detector sensitivity, and probe-sample coupling cancel out, and the true slope (due only to the medium's optical properties) is obtained.[53,59] Therefore, the SC method uses both SS measurements obtained with the source–detector combinations $S_1D_1D_2$ and $S_2D_2D_1$ and calculates the average of the two SS slopes. The retrieval of the optical properties is obtained iteratively.[7] Once these methods recover absolute μ_a, absolute $[HbO_2]$ and [HbR] are calculated with Beer's law and known extinction coefficients[60] of HbO_2 and HbR.

B. Measurement of changes in the absorption coefficient: The dual-slope (DS) method

The absolute optical properties measured with the SC method involve I and ϕ data types in combination. These two data types individually have different depth-sensitivities to $\Delta\mu_a$.[2] Therefore, we would mix information from different depths using the SC method to measure these changes. A straightforward depth-selective method to measure $\Delta\mu_a$ relies on only one data type (I or ϕ). For SD data, I will be mostly sensitive to changes occurring through superficial tissue, while ϕ data will be preferentially sensitive to deeper tissue (in the case of a semi-infinite homogeneous medium). The $\Delta\mu_a$'s can be measured with a single data type and with either SD or SS data by generalizing the concept of the differential path-length factor (DPF) for SD to the differential-slope factor (DSF) for SS.[6] By averaging the changes of two SSs, we obtain the dual-slope (DS) method,[54] which allows one to get rid of most instrumental confounds with the same reasoning as the SC method above. Here, we are using the DS method to translate changes of DS data into $\Delta\mu_a$'s according to the formula

$$\Delta\mu_{a,Y} = \frac{-[\Delta SS_{Y1} + \Delta SS_{Y2}]}{\langle L_2\rangle_{Y1} - \langle L_1\rangle_{Y1} + \langle L_2\rangle_{Y2} - \langle L_1\rangle_{Y2}}, \tag{5}$$

where $\Delta SS_{Y,i}$ is the change of slope i (where $i \in [1,2]$) and $\langle L_j\rangle_{Yi}$ is the generalized path-length at the distance j (where $j \in [1,2]$ for the short and long source–detector separation, respectively) of the slope i.[6] The $\Delta\mu_a$ may be recovered with either DS intensity (DSI) or DS phase (DSϕ) data; regardless, similar to above, $\Delta\mu_a$ is finally converted to $\Delta[HbO_2]$ and Δ[HbR] using Beer's law and known extinction coefficients.[60]

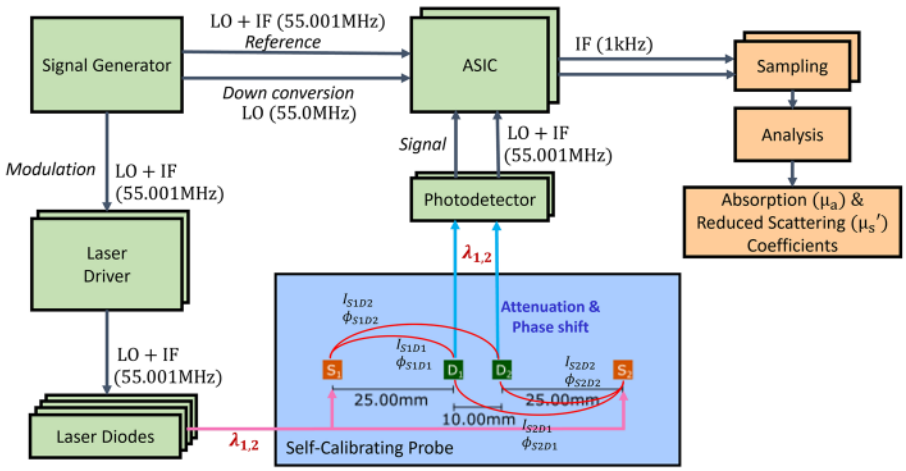

FIG. 1. Block diagram of the instrument showing all the major building blocks. The green color denotes all the components integrated onto a single PCB, the orange are the off-board blocks, and the blue block is the self-calibrating probe. LO: Local oscillator, IF: Intermediary Frequency, ASIC: Application Specific Integrated Circuit, $S_{1,2}$: Source locations, $D_{1,2}$: Detector locations, I: Intensity, ϕ: Phase.

20 March 2025 18:15:16

Published under an exclusive license by AIP Publishing

III. HARDWARE IMPLEMENTATION

In this work, we present a portable FD-NIRS instrument that employs heterodyne down-conversion using a single-frequency, multi-distance technique with time-division multiplexed light sources. The full instrument is shown in Fig. 2, consisting only of a printed circuit board of 14 × 17 cm^2, an STM32G491 microcontroller, and a Raspberry Pi 4. This system is designed for a DS probe configuration.

The key building blocks are shown in Fig. 1. For an FD-NIRS instrument employing heterodyne down-conversion, two radio frequencies (55.001 and 55.000 MHz in this case) that are separated by an intermediate frequency (IF = 1 kHz) are needed. The 55.001 MHz signal is used to modulate the intensity of the light sources. Therefore, the detected photon density wave from the medium will also be modulated at this frequency. With the heterodyne readout scheme, the information encoded in the recovered signal will be down-converted to a much lower frequency (i.e., IF). In this work, IF was chosen as 1 kHz. The reasoning behind this is that 1 kHz is low enough to be properly sampled by the STM32G491, while being high enough to be unaffected by low frequency noise sources like 1/f noise. This enables a much lower sampling rate compared to the direct sampling of the 55.001 MHz modulated signal, which would be significantly more expensive in terms of power consumption, unhelpful in terms of portability and require very powerful data processing solutions since the amount of data points generated would be directly correlated with the sampling speed.

An AD9959 Direct Digital Synthesizer (DDS) is used for signal generation. This component was selected due to its four output channels that are individually programmable (in frequency, amplitude, and phase), with very low phase noise (−110 dBc/Hz at 1 kHz offset with 75.1 MHz output frequency) and very high spectral purity characteristics (−87 dBc spurious free dynamic range at ±10 kHz offset with 75.1 MHz output frequency).[61] One of the output channels modulates the intensity of the four laser diodes through two laser driver circuits, each of which drives a pair of laser diodes of the same wavelength, 830 nm (HL8338MG, Thorlabs) or 690 nm (HL6750MG, Thorlabs). Another channel is fed into the ASICs as the reference signal against which the phase shift of the recovered signal is defined. The last two channels are used as the local oscillator signals. The laser driver circuits are a modified version of the well-known linear current regulator topology.[62] In this implementation, the circuit uses the monitoring current from the laser diodes, which is proportional to the optical power, to mitigate the effects of aging and thermal drifts.

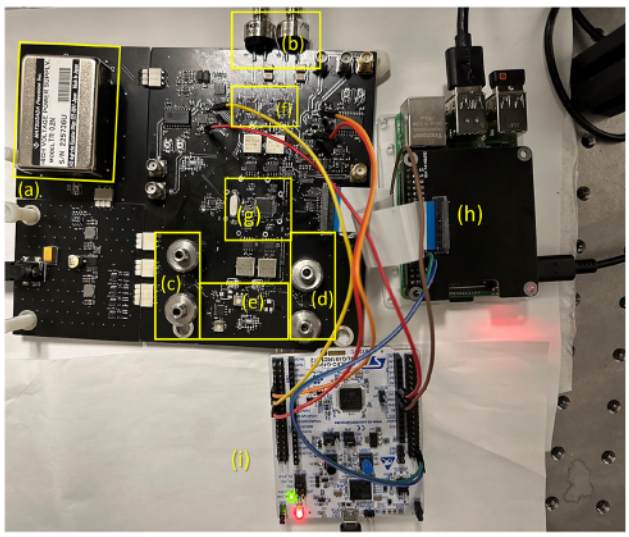

FIG. 2. Photo of the instrument. Panels show the following: (a) Avalanche Photo Diode (APD) supply, (b) APDs, (c) and (d) 830 and 690 nm lasers, respectively, (e) laser drivers, (f) application specific integrated circuits, (g) direct digital synthesizer, (h) Raspberry Pi 4, and (i) STM32G491 microcontroller.

The DS probe consists of two source locations and two detector locations, where the detector locations are sandwiched between the source locations. In this configuration, we have four source–detector combinations for each wavelength (as is typical for a DS set).[57] The geometry of the probe enables us to overcome systematic errors that are multiplicative in intensity and additive in phase[53,59] (see Sec. II). Two bifurcated optical fibers deliver light from two pairs of laser diodes (each pair comprising one laser at 690 nm and one at 830 nm) to the source locations on the probe (indicated with S_1 and S_2 in Fig. 1). In other words, each source location on the DS probe is connected to one laser diode at 690 nm and one at 830 nm.

During operation, each laser diode is alternately turned on for 50 ms, sending light to the source locations one at a time. After the light from the laser diodes gets attenuated and scattered in the tissue (medium), two fibers collect the light from the detector locations on the probe (D_1 and D_2 in Fig. 1) and guide the detected light to photodetectors.

Photodetectors used in this instrument are S9251-15 Avalanche Photo Diodes (APDs) from Hamamatsu. Even though photomultiplier tubes generally offer higher photosensitivity with lower noise levels than APDs, they operate under several kV biasing conditions, which makes them unsuitable for wearable or portable instruments. These APDs offer a high enough −3 dB bandwidth (350 MHz), low junction capacitance (3.6 pF), and 5000 A/W photosensitivity under only a −200 V biasing condition.

The low level electrical signals from the APDs (at 55.001 MHz) are then processed by the custom-designed, low noise analog front-end application-specific integrated circuit (ASIC), designed in a 130 nm IBM process.[52] Note that since there are two APDs, to process their outputs, either a switch to multiplex two APDs to a single ASIC is needed, or there needs to be one ASIC per APD. However, the former approach is unsuitable since the recovered light is on the order of nW to pW (considering a source on the order of mW), and the APD outputs are in the order of a few micro-amperes. The latter approach is selected since the ASICs will amplify any electronic noise contribution from additional components.

Each ASIC interfaces with one APD and amplifies its output current via a low noise transimpedance amplifier (TIA).[52] Then, the amplified signal is filtered to reject the out-of-band noise and finally down-converted to a 1 kHz signal. The ASIC uses the LO signal from the signal generator to accomplish the heterodyne down-conversion. The 1 kHz output signals contain all the information needed for the FD-NIRS, namely the intensity (I) and phase (ϕ) of the photon density wave recovered from the medium in the form of the amplitude and the phase shift of these electrical signals. At the penultimate stage, the 1 kHz output signals are sampled with the

20 March 2025 18:15:16

Published under an exclusive license by AIP Publishing

integrated analog-to-digital converters of an STM32G491 microcontroller to extract the intensity and phase information by applying fast Fourier transform (FFT) algorithms. Once the intensity and phase are gathered, they are sent to the final stage: a Raspberry Pi 4, for the computation of μ_a and μ_s' of the medium (see Sec. II). The Raspberry Pi 4 is also used to organize the time-division multiplexing, program the DDS, provide an interface for the user to control the experiment flow, and monitor the instrument's state. Sweeping all the lasers, sampling the outputs, and processing the data for one frame takes about 1.4 s, which corresponds to a 0.7 Hz acquisition rate per DS data point of intensity and phase of both wavelengths.

IV. RESULTS

A. Solid phantom measurements

The instrument was first tested on a solid tissue-mimicking phantom with known optical properties ($\mu_a \sim 0.006$ mm^{-1}, $\mu_s' \sim 0.7$ mm^{-1} at the wavelength of interest here). This solid phantom was fabricated in-house using titanium dioxide and India ink as scattering and absorbing components, respectively. Testing on a phantom allows one to characterize the instrument in terms of stability and noise as well as determine if its performance is suitable for *in vivo* experiments.

In Fig. 3, the measured intensity and phase of the ASICs' outputs from 690 nm sources for a 30 min long solid phantom experiment are presented. Figures 3(a)–3(d) show the intensity (I), and Figs. 3(e)–3(h) show the phase (ϕ) of all four combinations of the two sources and two detectors. Figure 3(i) shows changes in SS_1 and SS_2 for the $\ln[r^2 I]$ slope with respect to the first point for the two SSs and DS. Figure 3(j) shows the ϕ absolute SSs and DS. The intensity (I) and phase (ϕ) results are denoted with their source and detector designations, and SSs are denoted by which source they are obtained from (considering they utilize both detectors). For example, the two SS measurements for phase data are obtained from phase

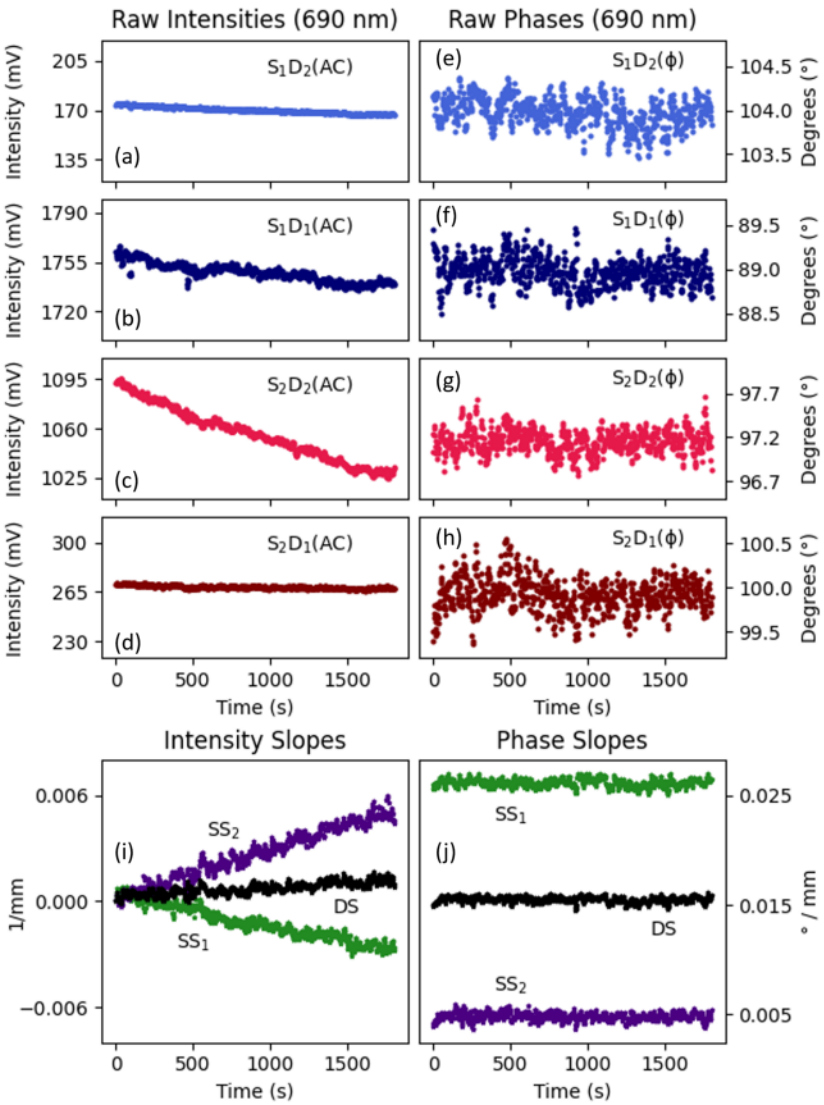

FIG. 3. Measured intensity and phase data from 690 nm sources during a half-hour phantom experiment. Panels (a) through (d) show the intensities, and (e) through (h) show the phases for different SDs (see Fig. 1). (i) shows the single-slope (SS) and dual-slope (DS) changes relative to the first time point for the intensities (I's), and (j) shows the absolute single-slopes (SSs) and the dual-slope (DS) for phase (ϕ).

20 March 2025 18:15:16

Published under an exclusive license by AIP Publishing

measurements at S_1D_1 and S_1D_2 (SS_1) and S_2D_2, S_2D_1 (SS_2). The average of these two SSs is the DS measurement. The same logic also follows for the intensity (I) data. As mentioned in Sec. II, the procedure from these measurements for the recovery of the optical properties is based on an iterative solution of the semi-infinite medium model of the diffuse reflectance and explained in detail by Blaney *et al.*[7]

The most important result in Fig. 3 is the apparent removal of instrumental drifts by the auto-calibration features of SC/DS. Due to thermal effects on the source and detector, all four intensities show varying degrees of drift, which is reflected as drift on SS_1 and SS_2 in Fig. 3(i). However, due to the properties of the SC/DS source–detector configuration, the drift of the two SSs cancels out when calculating DS. Note that in Fig. 3(i), the intensity slope changes with respect to the initial intensity slope (slope of $\ln[r^2 I]$) values were reported to demonstrate this auto-calibration feature of SC/DS geometries.[53,59] These initial absolute slopes are −0.164, −0.072, and −0.118 mm^{-1} for SS_1, SS_2, and DS, respectively.

Here, we use standard deviation to quantify the noise level of measured ϕ's and standard deviation over mean to quantify the noise over signal ratio for everything else (i.e., intensities I's, etc.). In this experiment, the average standard deviation over the mean for intensities from the 25 mm source–detector separation (S_1D_1 and S_2D_2) was 0.07%. For the 35 mm source–detector separation, this average relative error is 0.11% (S_1D_2 and S_2D_1). For the phase, the average standard deviation was measured to be 0.069° for the 25 mm source–detector separation and 0.082° for the 35 mm source–detector separation. It is worth noting that the stability metric (i.e., phase variation) is better for the signals obtained from 25 mm source–detector separations than 35 mm. This is expected since the recovered signals weaken as the separation increases and the noise-to-signal ratio becomes larger. Additionally, we have performed repeated probe placement experiments where we placed the probe on the phantom for 30 times. The instrument achieved a 3.5% standard deviation over the mean for intensity and 0.64° standard deviation for the phase at 25 mm source–detector separation and 3.3% standard deviation over the mean for intensity and 0.77° standard deviation for the phase at 35 mm source–detector separation.

Similarly, the recovered optical properties from this experiment can be seen in Fig. 4. In Figs. 4(a) and 4(b), the measured μ_a and μ_s' for both wavelengths are presented, respectively. For the recovered optical properties, the standard deviation over mean for μ_a was measured as 0.6% and 0.5% for 830 and 690 nm sources, respectively. For μ_s', this relative error was measured as 1% and 0.8% for 830 and 690 nm, respectively.

We have also compared the stability and drift performance of intensity and phase to the ISS Imagent V2 instrument. In terms of stability metrics mentioned before, Imagent V2 achieved 0.03% and 0.09% standard deviation over the mean for intensities for 25 and 35 mm source–detector separation, respectively, while our instrument had achieved 0.07% and 0.11%. For the phases, Imagent V2 achieved 0.013° and 0.043° standard deviation compared to our 0.069° and 0.082° for 25 and 35 mm separations, respectively. The drift in intensity for Imagent V2 was measured as 2.3% for 25 mm and 1.6% for 35 mm source–detector separations over a duration of 10 min. Our instrument has achieved 1.2% drift for 25 mm and 0.9% for 35 mm source–detector separations. For the phase drifts, Imagent V2's performance was 0.06° for 25 mm and 0.04° for 35 mm source–detector separation. This instrument achieved 0.02° for 25 mm and 0.04° for 35 mm source–detector separation. Even though we could match or surpass the Imagent V2 in terms of drift performance, these results show that there is still room for improvement for our instrument for stability.

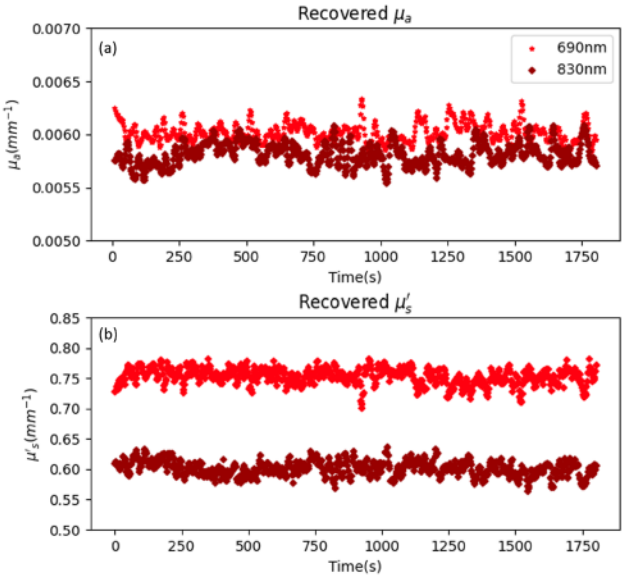

FIG. 4. (a) Measured absorption coefficient (μ_a) and (b) reduced scattering coefficient (μ_s') during a half-hour phantom experiment.

B. Vascular occlusion experiment

After characterizing the instrument on a solid phantom and verifying its capabilities, an *in vivo* vascular occlusion experiment was conducted on a healthy, 30-year-old male human subject in accordance with the Tufts University Institutional Review Board (IRB). In this experiment, an inflatable cuff was placed on the left upper arm. An inflated cuff pressure of 80 mmHg was applied, which is below arterial pressure but above venous pressure to induce a venous occlusion. The calculated radiant exposure to skin was calculated to be 97 mJ/cm^2, which is well within the requirements from ANSI Z136.1 laser safety standards.[4] The experimental procedure was as follows:

- The subject was seated on a chair with their left lower arm placed on a table, under the DS probe.
- The DS probe was positioned on the *brachioradialis* muscle, and an inflatable cuff was wrapped around the left upper arm.
- 5 mins of baseline optical data were collected.
- The cuff was inflated to 80 mmHg, and 3 min of occlusion data were collected.
- The cuff was deflated, and 2 min of recovery data were collected.

When the cuff is inflated, it is expected to occlude only the veins and not the arteries. Therefore, blood can enter the lower arm

20 March 2025 18:15:16

Published under an exclusive license by AIP Publishing

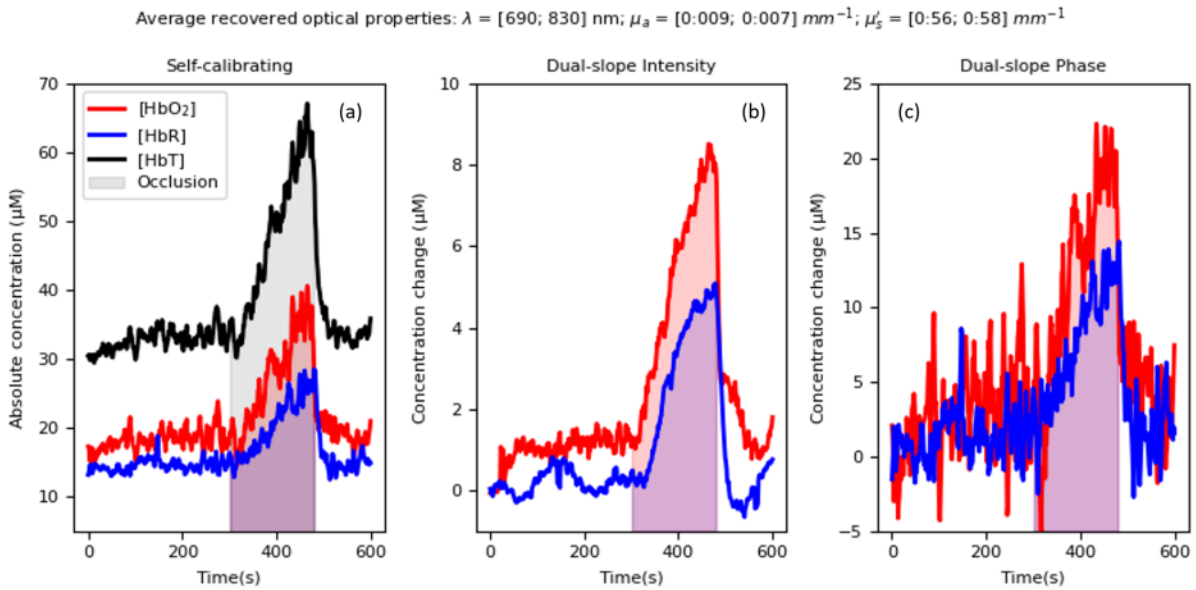

FIG. 5. Oxyhemoglobin ([HbO_2]), deoxyhemoglobin ([Hb]), and total-hemoglobin ([HbT]) concentrations during venous occlusion indicated by the shaded area. (a) Self-calibrating (SC) recovered absolute concentrations [see Fig. 6(a)]. (b) Dual-slope intensity (DSI) recovered concentration change. (c) Dual-slope phase (DSϕ) recovered concentration change.

in an oxygen-rich state through the unobstructed artery, yet it cannot leave the lower arm through the occluded veins. As a result, we expect to see a rise in both [HbO_2] and [HbR] in the lower arm as blood-volume increased.[63]

In Fig. 5, the measured [HbO_2] and [HbR], as well as their summation, total hemoglobin concentration ([HbT]; for absolute measurement with SC), are presented. The occlusion interval is indicated by the shaded region. It can be seen from Fig. 5 that during baseline (first 300 s), hemoglobin concentrations do not increase or decrease. When the occlusion starts, both [HbO_2] and [HbR] rise steadily until the cuff is released at 480 s, after which point the hemoglobin levels return to their baseline levels. The baseline tissue oxygen saturation (StO_2) level was measured as 60%, which is consistent with previously reported values for the human forearm.[64] Figure 5 shows three versions of these traces in three panels: the left panel shows the absolute concentrations recovered by SC,[53] the center panel shows the change in concentration recovered by DSI,[6,54] and the right panel shows the change in concentration recovered by DSϕ.[6,54] Differences between [HbO_2] and [HbR] traces recovered by DSI or DSϕ result from the data types' sensitivity to different regions within the tissue.[2,65] The SC recovered traces, on the other hand, are a combination of both I and ϕ data and allow μ_s' to vary with time (Fig. 6) while DS methods fix μ_s' (Sec. II).[6] Assuming μ_s' is fixed at a baseline value (as with DS methods) is more representative of the physiological reality, and the changes in the bottom panel of Fig. 6 (recovered by SC) are most likely an artifact resulting from cross-talk between absorption and scattering. Venous occlusion causes a large change in μ_a that may not be spatially homogeneous within the investigated tissue volume. Because in our analysis we treat the absorption change as spatially homogeneous, even a purely absorption change may result in an apparent scattering change as a result of cross-talk between the measured absorption and scattering changes.[66] While an increase in red blood cell concentration may result in greater optical scattering in tissue, the large scattering change (~20%) and its direction (decrease) observed in our experiment during venous occlusion is

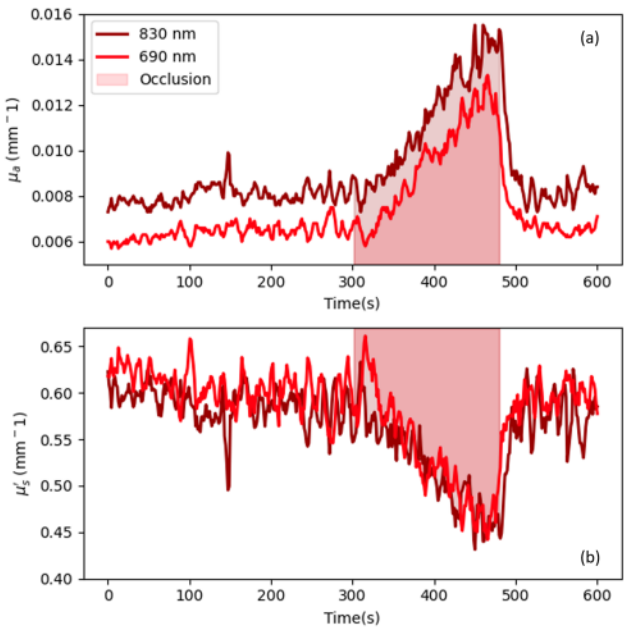

FIG. 6. Self-calibrating (SC) recovered absorption coefficient [μ_a; (a)] and reduced scattering coefficient [μ_s'; (b)] during venous occlusion, as indicated by the shaded area.

20 March 2025 18:15:16

Published under an exclusive license by AIP Publishing

assigned to a model-based cross-talk between measured absorption and scattering changes.

V. DISCUSSION

We have developed and validated a dual-wavelength, miniaturized frequency-domain near-infrared spectroscopy (FD-NIRS) instrument, focusing on its application in non-invasive measurements of oxyhemoglobin and deoxyhemoglobin concentrations in human tissues using dual-slope (DS) or self-calibrating (SC) techniques. This FD-NIRS system features an on-board signal generator, laser drivers with linear current control topology to modulate the intensity of laser diodes, and two APDs with corresponding custom-designed ASICs for heterodyne down-conversion and signal extraction. The instrument utilizes an STM32G491 microcontroller for digitization and a Raspberry Pi 4 for user interface, flow control, and computation. This work was a significant improvement over our previous iteration[51] on three aspects. First, we employed compact solutions such as an STM32G491 microcontroller for readout instead of a large data acquisition system from National Instruments. This removed a major obstacle against our ultimate goal of making a wearable instrument. Second, this instrument was also designed to be compatible with DS or SC techniques, which removes the need for pre-calibration for absolute measurements, and finally, the overall size of the instrument has been significantly reduced. Considering its compact design and DS/SC functionality, it is promising for applications in research and clinical settings.

We first conducted rigorous instrument testing using a solid phantom to assess its stability and noise performance. During the half-hour long solid phantom experiment, 0.08° phase noise and 0.11% standard deviation over mean for intensities were measured at a source–detector distance of 35 mm. These resulted in an average of 0.5% and 0.9% precision for the absorption and reduced scattering coefficients, respectively. We also compared our instrument's drift and stability characteristics to ISS Imagent V2 and found that in terms of drifting, our instrument performed better or was comparable in both intensity and phase for both 25 and 35 mm source–detector separations. However, there is still room for improvement for stability. These measurements suggested that the instrument would be appropriate for further human testing. Furthermore, the results illustrated the efficacy of the SC/DS technique in addressing systematic errors induced by thermal drifts and other instrumental or environmental factors. We confirmed the instrument's capability to measure hemodynamic changes effectively through subsequent *in vivo* testing with a vascular occlusion experiment on a healthy human subject. The occlusion pressure was picked to induce a venous occlusion. The experiment consisted of 5 min of baseline, 3 min of occlusion, and 2 min of recovery. In this experiment, we have successfully observed the absolute [HbO_2] and [HbR] to rise steadily during the occlusion and recover to their baseline levels after the occlusion was released. The dual-slope analysis performed separately on the intensity and phase data types showed some differences due to these two data types being more sensitive to different regions.[2]

We have also taken notice of several areas to be improved in the future. The acquisition rate of the instrument is currently not high enough to compare with many of the instruments in the literature. We believe the acquisition rate can be improved without modifying the hardware, but with software improvements. We located the major bottleneck to be the serial communication rate between the Raspberry Pi 4 and the STM32G491 microcontroller. Another shortcoming is the limited modulation frequency. Even though the signal generator can generate signals up to 250 MHz, the -3 dB bandwidth of our ASIC has been the reason behind using a modulation frequency of 55 MHz in this work. This relatively low modulation frequency compromises the phase contrast that the instrument can achieve since the phase difference between the source and the recovered light increases with increasing modulation frequency.[67] Assuming the additional integrated noise from the electronics due to higher bandwidth does not degrade the SNR of the data, a higher modulation frequency of the order of 100–150 MHz would be preferable. Finally, to accommodate for longer and shorter source–detector separations at the same time, a scheme allowing for larger dynamic range would be beneficial. The next significant milestone of this project is to tape out a new generation of ASIC. This would feature improved bandwidth (>100 MHz), a lower noise transimpedance amplifier, and most importantly, phase and amplitude readouts. Upon success, we believe the next major iteration of the instrument to consist of only the optics, DDS, a microcontroller, and the ASIC. Such an instrument can be of a wearable form factor.

VI. CONCLUSION

In this work, we have presented our new miniaturized, dual wavelength FD-NIRS instrument, featuring custom designed analog front-end ASICs designed in a 130 nm IBM process compatible with the dual-slope method. The instrument employs time division multiplexing to coordinate the light sources and detector readings and heterodyne down-conversion to ease the sampling requirements.

The instrument was first tested and characterized on a solid phantom with a half hour long continuous measurement. In this experiment, an average of 0.075° phase noise and 0.09% standard deviation over the mean for the intensities was achieved. These phase and intensity stability performances translated into 0.5% and 0.9% standard deviation over the mean for the μ_a and μ_s', respectively. During this Phantom experiment, the self-calibration feature of the dual-slope probe was also observed. After validating the instrument on a phantom, a vascular occlusion experiment on the brachioradialis muscle was performed. The cuff pressure was selected to induce venous occlusion, and the expected [HbO_2] and [HbR] trends during and after a venous occlusion were successfully observed. We have also discussed several shortcomings of the instrument. Some of these shortcomings could be mitigated without modifying the hardware but through software improvements, e.g., the bottleneck for the slow acquisition rate was determined to be the data rate between the Raspberry Pi 4 and the STM32G491 microcontroller. However, other shortcomings pointed us toward a new generation of the ASIC. This new generation would also mean further integration, such as the phase and amplitude readout. Another possible future improvement on this device would be to slightly modify the probe configuration to allow for multi-distance data acquisition.

To summarize, we present a portable DS FD-NIRS instrument for non-invasive optical measurements of hemoglobin concentrations. It is a valuable tool with potential for various biomedical applications, including functional brain imaging, neonatal care, and

20 March 2025 18:15:16

Published under an exclusive license by AIP Publishing

disease diagnosis through tissue oxygenation. In the future, we will focus on further miniaturization through a new generation of ASIC and expand the range of clinical applications to realize the potential of this innovative DS FD-NIRS system.

ACKNOWLEDGMENTS

This work was supported by the National Institutes of Health (NIH) Award No. R01-EB029414. G.B. would also like to acknowledge support from NIH Award No. K12-GM133314. The content is solely the authors' responsibility and does not necessarily represent the official views of the awarding institutions. We would like to acknowledge Dr. B. Kabagöz for his insightful discussions.

This study has been reviewed and approved by Tufts University Institutional Review Board (IRB, No. STUDY00000277).

AUTHOR DECLARATIONS

Conflict of Interest

The authors have no conflicts to disclose.

Author Contributions

Alper Kılıç: Conceptualization (equal); Data curation (lead); Formal analysis (lead); Investigation (lead); Methodology (lead); Software (lead); Validation (lead); Visualization (lead); Writing – original draft (lead); Writing – review & editing (lead). **Giles Blaney**: Formal analysis (equal); Funding acquisition (supporting); Visualization (supporting); Writing – original draft (supporting); Writing – review & editing (equal). **Fatemeh Tavakoli**: Data curation (supporting); Writing – review & editing (supporting). **Jodee Frias**: Writing – review & editing (supporting). **Angelo Sassaroli**: Formal analysis (supporting); Methodology (supporting); Validation (supporting); Writing – original draft (supporting); Writing – review & editing (equal). **Sergio Fantini**: Funding acquisition (equal); Investigation (supporting); Methodology (supporting); Project administration (equal); Resources (equal); Supervision (equal); Writing – original draft (supporting); Writing – review & editing (equal). **Valencia Koomson**: Conceptualization (equal); Funding acquisition (equal); Investigation (supporting); Methodology (supporting); Project administration (equal); Resources (equal); Supervision (equal); Writing – original draft (supporting); Writing – review & editing (equal).

DATA AVAILABILITY

The data that support the findings of this study are available from the corresponding author upon reasonable request.

REFERENCES

[1]H. Ayaz, W. B. Baker, G. Blaney, D. A. Boas, H. Bortfeld, K. Brady, J. Brake, S. Brigadoi, E. M. Buckley, S. A. Carp, R. J. Cooper, K. R. Cowdrick, J. P. Culver, I. Dan, H. Dehghani, A. Devor, T. Durduran, A. T. Eggebrecht, L. L. Emberson, Q. Fang, S. Fantini, M. A. Franceschini, J. B. Fischer, J. Gervain, J. Hirsch, K.-S. Hong, R. Horstmeyer, J. M. Kainerstorfer, T. S. Ko, D. J. Licht, A. Liebert, R. Luke, J. M. Lynch, J. Mesquida, R. C. Mesquita, N. Naseer, S. L. Novi, F. Orihuela-Espina, T. D. O'Sullivan, D. S. Peterka, A. Pifferi, L. Pollonini, A. Sassaroli, J. R. Sato, F. Scholkmann, L. Spinelli, V. J. Srinivasan, K. St Lawrence, I. Tachtsidis, Y. Tong, A. Torricelli, T. Urner, H. Wabnitz, M. Wolf, U. Wolf, S. Xu, C. Yang, A. G. Yodh, M. A. Yücel, and W. Zhou, "Optical imaging and spectroscopy for the study of the human brain: Status report," Neurophotonics **9**, S24001 (2022).

[2]G. Blaney, A. Sassaroli, and S. Fantini, "Spatial sensitivity to absorption changes for various near-infrared spectroscopy methods: A compendium review," J. Innovative Opt. Health Sci. **17**, 2430001 (2024).

[3]S. Feng, F.-A. Zeng, and B. Chance, "Photon migration in the presence of a single defect: A perturbation analysis," Appl. Opt. **34**, 3826–3837 (1995).

[4]I. J. Bigio and S. Fantini, *Quantitative Biomedical Optics: Theory, Methods, and Applications* (Cambridge University Press, Cambridge, 2016).

[5]S. Fantini and A. Sassaroli, "Frequency-domain techniques for cerebral and functional near-infrared spectroscopy," Front. Neurosci. **14**, 300 (2020).

[6]G. Blaney, A. Sassaroli, T. Pham, C. Fernandez, and S. Fantini, "Phase dual-slopes in frequency-domain near-infrared spectroscopy for enhanced sensitivity to brain tissue: First applications to human subjects," J. Biophot. **13**, e201960018 (2020).

[7]G. Blaney, R. Donaldson, S. Mushtak, H. Nguyen, L. Vignale, C. Fernandez, T. Pham, A. Sassaroli, and S. Fantini, "Dual-slope diffuse reflectance instrument for calibration-free broadband spectroscopy," Appl. Sci. **11**, 1757 (2021).

[8]R. Durbha and V. Koomson, "Chromasense-empowering health, empowering you [innovations corner]," IEEE Circuits Syst. Mag. **24**, 45–46 (2024).

[9]F. F. Jöbsis, "Noninvasive, infrared monitoring of cerebral and myocardial oxygen sufficiency and circulatory parameters," Science **198**, 1264–1267 (1977).

[10]P.-Y. Lin, N. Roche-Labarbe, M. Dehaes, S. Carp, A. Fenoglio, B. Barbieri, K. Hagan, P. Grant, and M. A. Franceschini, "Non-invasive optical measurement of cerebral metabolism and hemodynamics in infants," J. Visualized Exp. (73), e4379 (2013).

[11]S. Fantini, E. L. Heffer, H. Siebold, and O. Schütz, "Using near-infrared light to detect breast cancer," Opt. Photonics News **14**, 24–29 (2003).

[12]P.-Y. Lin, K. Hagan, A. Fenoglio, P. Grant, and M. A. Franceschini, "Reduced cerebral blood flow and oxygen metabolism in extremely preterm neonates with low-grade germinal matrix- intraventricular hemorrhage," Sci. Rep. **6**, 25903 (2016).

[13]M. Calderon-Arnulphi, A. Alaraj, S. Amin-Hanjani, W. Mantulin, C. Polzonetti, E. Gratton, and F. Charbel, "Detection of cerebral ischemia in neurovascular surgery using quantitative frequency-domain near-infrared spectroscopy," J. Neurosurg. **106**, 283–290 (2007).

[14]E. S. Papazoglou, M. T. Neidrauer, L. Zubkov, M. S. Weingarten, and K. Pourrezaei, "Noninvasive assessment of diabetic foot ulcers with diffuse photon density wave methodology: Pilot human study," J. Biomed. Opt. **14**, 064032 (2009).

[15]M. A. Khalil, H. K. Kim, I.-K. Kim, M. Flexman, R. Dayal, G. Shrikhande, and A. H. Hielscher, "Dynamic diffuse optical tomography imaging of peripheral arterial disease," Biomed. Opt. Express **3**, 2288–2298 (2012).

[16]F. Scholkmann, S. Kleiser, A. J. Metz, R. Zimmermann, J. Mata Pavia, U. Wolf, and M. Wolf, "A review on continuous wave functional near-infrared spectroscopy and imaging instrumentation and methodology," NeuroImage **85**, 6–27 (2014).

[17]Y. Yamada, H. Suzuki, and Y. Yamashita, "Time-domain near-infrared spectroscopy and imaging: A review," Appl. Sci. **9**, 1127 (2019).

[18]S. Fantini, M.-A. Franceschini, J. S. Maier, S. A. Walker, B. B. Barbieri, and E. Gratton, "Frequency-domain multichannel optical detector for noninvasive tissue spectroscopy and oximetry," Opt. Eng. **34**, 32–42 (1995).

[19]S. A. Carp, P. Farzam, N. Redes, D. M. Hueber, and M. A. Franceschini, "Combined multi-distance frequency domain and diffuse correlation spectroscopy system with simultaneous data acquisition and real-time analysis," Biomed. Opt. Express **8**, 3993–4006 (2017).

[20]B. J. Tromberg, N. Shah, R. Lanning, A. Cerussi, J. Espinoza, T. Pham, L. Svaasand, and J. Butler, "Non-invasive in vivo characterization of breast tumors using photon migration spectroscopy," Neoplasia **2**, 26–40 (2000).

[21]A. Orlova, I. Turchin, V. Plehanov, N. Shakhova, I. Fiks, M. Kleshnin, N. Konuchenko, and V. Kamensky, "Frequency-domain diffuse optical tomography with single source-detector pair for breast cancer detection," Laser Phys. Lett. **5**, 321–327 (2008).

20 March 2025 18:15:16

Published under an exclusive license by AIP Publishing

[22]T. D. O'Sullivan, A. E. Cerussi, D. J. Cuccia, and B. J. Tromberg, "Diffuse optical imaging using spatially and temporally modulated light," J. Biomed. Opt. **17**, 0713111 (2012).
[23]T. H. Pham, O. Coquoz, J. B. Fishkin, E. Anderson, and B. J. Tromberg, "Broad bandwidth frequency domain instrument for quantitative tissue optical spectroscopy," Rev. Sci. Instrum. **71**, 2500–2513 (2000).
[24]D. Roblyer, T. D. O'Sullivan, R. V. Warren, and B. Tromberg, "Feasibility of direct digital sampling for diffuse optical frequency domain spectroscopy in tissue," Meas. Sci. Technol. **24**, 045501 (2013).
[25]A. Torjesen, R. Istfan, and D. Roblyer, "Ultrafast wavelength multiplexed broad bandwidth digital diffuse optical spectroscopy for in vivo extraction of tissue optical properties," J. Biomed. Opt. **22**, 036009 (2017).
[26]B. B. Zimmermann, Q. Fang, D. A. Boas, and S. A. Carp, "Frequency domain near-infrared multiwavelength imager design using high-speed, direct analog-to-digital conversion," J. Biomed. Opt. **21**, 016010 (2016).
[27]R. A. Stillwell, V. J. Kitsmiller, A. Y. Wei, A. Chong, L. Senn, and T. D. O'Sullivan, "A scalable, multi-wavelength, broad bandwidth frequency-domain near-infrared spectroscopy platform for real-time quantitative tissue optical imaging," Biomed. Opt. Express **12**, 7261–7279 (2021).
[28]G. Yu, T. Durduran, D. Furuya, J. H. Greenberg, and A. G. Yodh, "Frequency-domain multiplexing system for in vivo diffuse light measurements of rapid cerebral hemodynamics," Appl. Opt. **42**, 2931–2939 (2003).
[29]T. O. McBride, B. W. Pogue, S. Jiang, U. L. Österberg, and K. D. Paulsen, "A parallel-detection frequency-domain near-infrared tomography system for hemoglobin imaging of the breast in vivo," Rev. Sci. Instrum. **72**, 1817–1824 (2001).
[30]H. Liu, H. Liu, X. Li, and B. Chance, "Low-cost frequency-domain photon migration instrument for tissue spectroscopy, oximetry, and imaging," Opt. Eng. **36**, 1562–1569 (1997).
[31]Q. Zhang, T. J. Brukilacchio, A. Li, J. J. Stott, T. Chaves, E. M. C. Hillman, T. Wu, M. Chorlton, E. A. Rafferty, R. H. Moore, D. B. Kopans, and D. A. Boas, "Coregistered tomographic x-ray and optical breast imaging: Initial results," J. Biomed. Opt. **10**, 024033 (2005).
[32]J. P. Culver, R. Choe, M. J. Holboke, L. Zubkov, T. Durduran, A. Slemp, V. Ntziachristos, B. Chance, and A. G. Yodh, "Three-dimensional diffuse optical tomography in the parallel plane transmission geometry: Evaluation of a hybrid frequency domain/continuous wave clinical system for breast imaging," Med. Phys. **30**, 235–247 (2003).
[33]Y. Yu, N. Liu, A. Sassaroli, and S. Fantini, "Near-infrared spectral imaging of the female breast for quantitative oximetry in optical mammography," Appl. Opt. **48**, D225–D235 (2009).
[34]N. G. Chen, M. Huang, H. Xia, D. Piao, E. Cronin, and Q. Zhu, "Portable near-infrared diffusive light imager for breast cancer detection," J. Biomed. Opt. **9**, 504–510 (2004).
[35]K.-S. No, R. Kwong, P. H. Chou, and A. Cerussi, "Design and testing of a miniature broadband frequency domain photon migration instrument," J. Biomed. Opt. **13**, 050509 (2008).
[36]B. W. Pogue, M. Testorf, T. McBride, U. Osterberg, and K. Paulsen, "Instrumentation and design of a frequency-domain diffuse optical tomography imager for breast cancer detection," Opt. Express **1**, 391–403 (1997).
[37]J. Rey, R. Mackey, R. T. Powis, J. C. Walton, K. M. Hauser, C. S. Hall, D. J. Gotti, and A. R. Harrivel, Frequency domain functional near-infrared spectrometer (fNIRS) for crew state monitoring (2020).
[38]B. W. Pogue *et al.*, "A 32-channel frequency-domain fNIRS system based on silicon photomultiplier receivers," Proc. SPIE **11629**, 116291P (2021).
[39]M. C. Thompson *et al.*, "Phase component of frequency-domain functional near-infrared imaging improves decoding of motor-evoked neural activity," in *International IEEE/EMBS Conference on Neural Engineering, NER 2021-May* (IEEE, 2021), pp. 365–369.
[40]P.-T. Lee, H.-C. Chang, Y.-F. Hsu, H. Jiang, and M.-C. Pan, "Simultaneous multiple frequency and flexible optical channels based doi system," Proc. SPIE **11952**, 119520A (2022).
[41]S. Yazdi, S. Mohammadi, S. Lahade, A. Beck, T. Quang, J. H. Lam, T. D. O'Sullivan, and M. M. Green, "Broad-bandwidth frequency-domain near-infrared spectroscopy system on a chip," Proc. SPIE **11956**, 1195603 (2022).
[42]B. J. Koh and H. M. Bae, "Multimodal portable functional brain imaging chip," IDEC J. Integr. Circuits Syst. **8**, 49 (2022).
[43]C. Chen, Z. Ma, Y. Liu, Z. Liu, L. Zhou, Y. Wu, L. Qi, Y. Li, M. Sawan, G. Wang, and J. Zhao, "A sub-0.01° phase resolution 6.8-mw fNIRS readout circuit employing a mixer-first frequency-domain architecture," in *ESSCIRC 2022—IEEE 48th European Solid State Circuits Conference, Proceedings* (IEEE, 2022), pp. 229–232.
[44]R. Yun and V. M. Joyner, "Design of an integrated sensor for noninvasive optical mammography based on frequency-domain NIR spectroscopy," in *2008 IEEE-BIOCAS Biomedical Circuits and Systems Conference, BIOCAS 2008* (IEEE, 2008), pp. 185–188.
[45]R. Yun and V. M. Joyner, "A monolithically integrated phase-sensitive optical sensor for frequency-domain NIR spectroscopy," IEEE Sens. J. **10**, 1234–1242 (2010).
[46]R. Yun and V. J. Koomson, "A novel CMOS frequency-mixing transimpedance amplifier for frequency domain near infrared spectroscopy," IEEE Trans. Circuits Syst. I: Regular Pap. **60**, 84–94 (2013).
[47]C. C. Sthalekar and V. J. Koomson, "A CMOS sensor for measurement of cerebral optical coefficients using non-invasive frequency domain near infrared spectroscopy," IEEE Sens. J. **13**, 3166–3174 (2013).
[48]C. C. Sthalekar, Y. Miao, and V. J. Koomson, "Optical characterization of tissue phantoms using a silicon integrated fdNIRS system on chip," IEEE Trans. Biomed. Circuits Syst. **11**, 279–286 (2017).
[49]Y. Miao and V. J. Koomson, "A CMOS integrated fdNIRS and TDCS system for simultaneous brain stimulation and monitoring," in *Midwest Symposium on Circuits and Systems 2017-August* (IEEE, 2017), pp. 499–502.
[50]Y. Miao and V. J. Koomson, "A cmos-based bidirectional brain machine interface system with integrated fdNIRS and tDCS for closed-loop brain stimulation," IEEE Trans. Biomed. Circuits Syst. **12**, 554–563 (2018).
[51]A. Kılıç, Y. Miao, and V. Koomson, "Design of a miniaturized frequency domain near infrared spectrometer with validation in solid phantoms and human tissue," J. Near Infrared Spectrosc. **31**, 3–13 (2023).
[52]Y. Miao and V. J. Koomson, "A CMOS integrated fdNIRS and TDCS system for simultaneous brain stimulation and monitoring," in *2017 IEEE 60th International Midwest Symposium on Circuits and Systems (MWSCAS)* (IEEE, 2017), pp. 499–502.
[53]D. M. Hueber, S. Fantini, A. E. Cerussi, and B. B. Barbieri, "New optical probe designs for absolute (self-calibrating) NIR tissue hemoglobin measurements," SPIE Proc. **3597**, 618–631 (1999).
[54]A. Sassaroli, G. Blaney, and S. Fantini, "Dual-slope method for enhanced depth sensitivity in diffuse optical spectroscopy," J. Opt. Soc. Am. A **36**, 1743–1761 (2019).
[55]S. Fantini, M. A. Franceschini, J. B. Fishkin, B. Barbieri, and E. Gratton, "Quantitative determination of the absorption spectra of chromophores in strongly scattering media: A light-emitting-diode based technique," Appl. Opt. **33**, 5204–5213 (1994).
[56]M. B. Applegate, C. A. Gómez, and D. M. Roblyer, "Modulation frequency selection and efficient look-up table inversion for frequency domain diffuse optical spectroscopy," J. Biomed. Opt. **26**, 036007 (2021).
[57]G. Blaney, A. Sassaroli, and S. Fantini, "Design of a source–detector array for dual-slope diffuse optical imaging," Rev. Sci. Instrum. **91**, 093702 (2020).
[58]S. Fantini, D. Hueber, M. A. Franceschini, E. Gratton, W. Rosenfeld, P. G. Stubblefield, D. Maulik, and M. R. Stankovic, "Non-invasive optical monitoring of the newborn piglet brain using continuous-wave and frequency-domain spectroscopy," Phys. Med. Biol. **44**, 1543–1563 (1999).
[59]G. Blaney, A. Sassaroli, C. Fernandez, M. Bottoni, and S. Fantini, "Functional brain mapping with dual-slope frequency-domain near-infrared spectroscopy," Proc. SPIE **11946**, 1194602 (2022).
[60]S. Jacques, Extinction Coefficient of Melanin (2018); https://omlc.org/spectra/melanin/extcoeff.html
[61]4-Channel, 500 MSPS DDS with 10-Bit DACs, Analog Devices, rev. C (2005).

20 March 2025 18:15:16

Published under an exclusive license by AIP Publishing

[62]Z. Richards, "How to generate current sources and sinks of arbitrary magnitude," Technical Report (Texas Instruments, 2015).
[63]R. A. De Blasi, M. Ferrari, A. Natali, G. Conti, A. Mega, and A. Gasparetto, "Noninvasive measurement of forearm blood flow and oxygen consumption by near-infrared spectroscopy," J. Appl. Physiol. **76**, 1388–1393 (1994).
[64]G. Blaney, P. Curtsmith, A. Sassaroli, C. Fernandez, and S. Fantini, "Broadband absorption spectroscopy of heterogeneous biological tissue," Appl. Opt. **60**, 7552–7562 (2021).
[65]C. Fernandez, G. Blaney, J. Frias, F. Tavakoli, A. Sassaroli, and S. Fantini, "Single-distance and dual-slope frequency-domain near-infrared spectroscopy to assess skeletal muscle hemodynamics," J. Biomed. Opt. **28**, 125004 (2023).
[66]L. Yang, H. Wabnitz, T. Gladytz, R. Macdonald, and D. Grosenick, "Spatially-enhanced time-domain NIRS for accurate determination of tissue optical properties," Opt. Express **27**, 26415–26431 (2019).
[67]J. R. Lakowicz and K. Berndt, "Frequency-domain measurements of photon migration in tissues," Chem. Phys. Lett. **166**, 246–252 (1990).

20 March 2025 18:15:16

Published under an exclusive license by AIP Publishing